Special Issue

Posterior Eye Shape Measurement With Retinal OCT Compared to MRI

Anthony N. Kuo,[1] Pavan K. Verkicharla,[2] Ryan P. McNabb,[1] Carol Y. Cheung,[3] Saima Hilal,[4] Sina Farsiu,[1,5] Christopher Chen,[4] Tien Y. Wong,[2,6,7] M. Kamran Ikram,[4,8] Ching Y. Cheng,[2,6] Terri L. Young,[6,9] Seang M. Saw,[2,6] and Joseph A. Izatt[1,5]

[1]Department of Ophthalmology, Duke University Medical Center, Durham, North Carolina, United States
[2]Singapore Eye Research Institute, The Academia, Singapore
[3]Department of Ophthalmology and Visual Sciences, The Chinese University of Hong Kong, Hong Kong
[4]Memory Aging & Cognition Centre and Department of Pharmacology, National University of Singapore, Singapore
[5]Department of Biomedical Engineering, Duke University, Durham, North Carolina, United States
[6]Duke-National University of Singapore (NUS) Graduate Medical School, Singapore, Singapore
[7]Singapore National Eye Centre, Singapore, Singapore
[8]Department of Epidemiology, Erasmus University Medical Center, Rotterdam, The Netherlands
[9]University of Wisconsin-Madison, Department of Ophthalmology and Visual Sciences, Madison, Wisconsin, United States

Correspondence: Anthony N. Kuo, Duke Eye Center, DUMC Box 3802, Durham, NC 27710, USA; anthony.kuo@duke.edu.

Submitted: December 13, 2015
Accepted: March 20, 2016

Citation: Kuo AN, Verkicharla PK, McNabb RP, et al. Posterior eye shape measurement with retinal OCT compared to MRI. *Invest Ophthalmol Vis Sci*. 2016;57:OCT196–OCT203. DOI:10.1167/iovs.15-18886

Purpose. Posterior eye shape assessment by magnetic resonance imaging (MRI) is used to study myopia. We tested the hypothesis that optical coherence tomography (OCT), as an alternative, could measure posterior eye shape similarly to MRI.

Methods. Macular spectral-domain OCT and brain MRI images previously acquired as part of the Singapore Epidemiology of Eye Diseases study were analyzed. The right eye in the MRI and OCT images was automatically segmented. Optical coherence tomography segmentations were corrected for optical and display distortions requiring biometry data. The segmentations were fitted to spheres and ellipsoids to obtain the posterior eye radius of curvature (R_c) and asphericity (Q_{xz}). The differences in R_c and Q_{xz} measured by MRI and OCT were tested using paired *t*-tests. Categorical assignments of prolateness or oblateness using Q_{xz} were compared.

Results. Fifty-two subjects (67.8 ± 5.6 years old) with spherical equivalent refraction from +0.50 to −5.38 were included. The mean paired difference between MRI and original OCT posterior eye R_c was 24.03 ± 46.49 mm ($P = 0.0005$). For corrected OCT images, the difference in R_c decreased to −0.23 ± 2.47 mm ($P = 0.51$). The difference between MRI and OCT asphericity, Q_{xz}, was −0.052 ± 0.343 ($P = 0.28$). However, categorical agreement was only moderate ($\kappa = 0.50$).

Conclusions. Distortion-corrected OCT measurements of R_c and Q_{xz} were not statistically significantly different from MRI, although the moderate categorical agreement suggests that individual differences remained. This study provides evidence that with distortion correction, noninvasive office-based OCT could potentially be used instead of MRI for the study of posterior eye shape.

Keywords: optical coherence tomography, magnetic resonance imaging, asphericity, myopia

Myopia is a common condition affecting a large percentage of individuals worldwide, ranging from 30% to 90% depending on the age of the population (more common in younger populations), ethnicity (more common in Chinese, Japanese, Koreans), and region (more common in urban cities in Asia).[1–5] It has been shown that eye shape in individuals with myopia—especially those with high myopia and pathologic myopia—differs compared to that in emmetropic individuals.[6–8] Furthermore, different types of posterior eye shape are associated with pathologic forms of myopia with vision-threatening complications.[9–11] These pathologic forms of myopia are a major cause of vision loss, particularly in Asian countries. Understanding structural changes in myopia can provide insight into mechanisms and hence help in development of prevention strategies.

The vast majority of studies investigating posterior eye shape have been performed with magnetic resonance imaging (MRI).[6–8,12,13] While MRI provides a complete three-dimensional (3D) representation of the entire eye free of optical distortions, there are logistical and financial barriers to readily obtaining MRI images of the eye on a routine basis, limiting the current use of posterior eye shape primarily to highly specialized research settings. Developing techniques as alternatives to MRI would make measurement of posterior eye shape more accessible to both researchers and clinicians and may allow better understanding of the structural changes that lead to pathologic myopia.

Since its invention, optical coherence tomography (OCT) has become a readily available and indispensable 3D ocular imaging technique in widespread use in eye clinics and research centers worldwide.[14,15] Optical coherence tomogra-

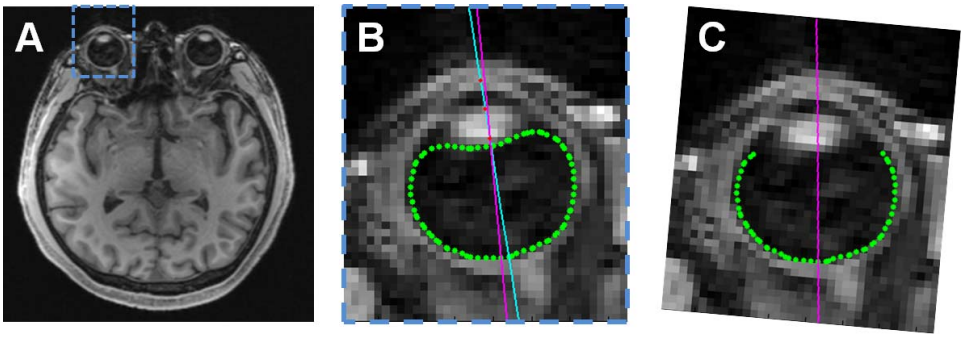

FIGURE 1. Overview of analysis of MRI images. (**A**) The right eyes from 1-mm isotropic axial MPRAGE slices were analyzed. (**B**) Magnified view of *blue-bounded box* in (**A**). The vitreous/eye wall boundary was automatically segmented (*green*) and a user-defined optical axis through the corneal apex, anterior lens apex, and posterior lens apex was created (*red dots* and *light blue line*). The visual axis (*magenta*) was defined as 3.5° temporal to the optical axis relative to the posterior lens apex. (**C**) The eye was rotated so that the visual axis was parallel to the *z* (anterior–posterior) axis. The posterior 240° of the segmented volume was then fit to the desired shape. (Segmentations from the other slices comprising the right eye volume are not shown here).

phy images of the eye, however, suffer from distortions that affect OCT's ability to accurately represent the shape of the eye.[16–20] Briefly, these distortions result from refraction of OCT light through the eye and from display of nontelecentric scans on a rectangular format. When these optical and display distortions are corrected, the difference between OCT- and MRI-measured posterior eye shape expressed as spherical radius of curvature is decreased.[20]

The objective of this study was to test the hypothesis that distortion-corrected OCT images of the posterior eye would produce similar measurements of both spherical and aspherical posterior eye shape compared to MRI images of the same eyes. Optical coherence tomography and MRI images previously acquired as part of a national epidemiologic study were used for this study. This was a unique dataset because the OCT data were acquired using a common, commercially available OCT system. Further, instead of a highly controlled acquisition protocol specific for shape, these OCT images were acquired using regular clinical protocols and therefore are broadly applicable as a reflection of general OCT usage.

METHODS

Subject Selection

The study dataset was drawn from subjects who had previously enrolled in the Singapore Epidemiology of Eye Diseases (SEED) study and its Epidemiology of Dementia in Singapore (EDIS) substudy.[3,21–24] Both were multiethnic, population-based studies of 40- to 85-year-old Singaporeans. For the SEED and EDIS studies, the research followed the tenets of the Declaration of Helsinki; informed consent was obtained from the subjects after explanation of the nature and possible consequences of the study; and the research was approved by the SingHealth Institutional Review Board (IRB) and the National Healthcare Group Domain-Specific Review Board. For the current retrospective study, the research followed the tenets of the Declaration of Helsinki, and the research was additionally approved by the Duke University Medical Center IRB.

A total of 251 subjects who had undergone both ocular OCT scans and brain MRI scans in the SEED study and EDIS substudy were initially included. From this population, subjects with a spherical equivalent refraction of +0.50 or more myopic were chosen to include emmetropic and myopic individuals (101 subjects from the initial population). Subjects were then excluded if there was no macular OCT scan (macular scans were used for OCT analysis: −13 subjects), if they were pseudophakic (pseudophakic refraction may not reflect the original refractive error of the eye: −23 subjects), or if they lacked ocular biometric values (required for OCT distortion correction in this study: −13 subjects). A final total of 52 subject datasets met all the inclusion and exclusion criteria and proceeded to analysis.

MRI Analysis

The MRI images (3T Magnetom Trio Tim; Siemens, Munich, Germany) were previously acquired using a 32-channel head coil at the Clinical Imaging Research Centre of the National University of Singapore. The standardized protocol included high-resolution, 3D T1-weighted Magnetization Prepared Rapid Gradient Recalled Echo (MPRAGE) sequences with 1.0-× 1.0-× 1.0-mm^3 voxels, repetition time (TR) = 7.2 ms, time to echo (TE) = 3.3 ms, inversion time (TI) = 900 ms, flip angle = 9°, and matrix = 256 × 256 × 180 mm^3.

For MRI analysis, axial slices were created from the 1-mm isotropic MPRAGE volumes to match the orientation of the axial OCT scans. The slices were exported as bitmap image stacks for analysis. Using active contours[25] implemented in MATLAB (MathWorks; Natick, MA, USA), the interface between the dark vitreous and bright eye wall was automatically segmented in each slice containing the right eye; the search region was initially limited by manual designation of two opposite corners of a box encompassing the eye (similar to Fig. 1B) and an arbitrary point within the vitreous. In the axial slice containing both the lens and optic nerve, an optical axis was defined by manual designation and linear fitting of three points: apex of the anterior cornea, apex of the anterior lens, and apex of the posterior lens. Relative to this optical axis, all images were rotated by 3.5° in the axial plane so that the posterior eye shape was estimated with reference to the visual axis that passed through the fovea (*z*-axis).[26] This estimate of "visual axis" was required because there was insufficient resolution in the MRI scans to visualize the fovea directly; the difference between the visual and optical axis in an older population similar to ours was approximately 3.5°.[27] The anterior 120° containing the cornea and lens was then removed.[28] Hence the posterior 240° of the eye with visual axis coincident with the *z*-axis was the final form used for shape analysis (Fig. 1). (In this work, the axis designations are *x*-axis: left–right lateral axis, *y*-axis: cranial–caudal axis, and *z*-axis: anterior–posterior axis. Using this axis designation, the axial plane is the *xz* plane, the coronal plane is the *xy* plane, and the sagittal plane is the *yz* plane).

OCT Analysis

Nominally 6- × 6-mm macular OCT (Cirrus; Zeiss, Jena, Germany) scan volumes of the dilated right eye composed of 1024 depth pixels × 512 A-scans × 128 B-scans were used for OCT analysis. We imported the OCT volumes into a custom, automated layer segmentation software—the Duke OCT Retinal Analysis Program (DOCTRAP). The core automated segmentation algorithm of DOCTRAP is based on the graph theory and dynamic programming framework.[29] Using DOCTRAP, the retinal pigment epithelium (RPE) was automatically segmented within each axial B-scan. Optical and display distortions were then removed using a numeric distortion correction algorithm based on an optical model of the OCT scanner and patient eye implemented in OpticStudio Standard (Zemax, LLC, Kirkland, WA, USA).[20]

Regarding the OCT scanner in the model, an important step was calibrating the scan dimensions of the specific OCT system used to acquire the retinal OCT data. Achromatic focusing lenses (Thorlabs, Inc.; Newton, NJ, USA) were mounted in front of the Cirrus used in the SEED study to focus the retinal scan beam to a micrometer target (Newport Corp., Irvine, CA, USA). A 1024- × 512- × 128-pixel volume was taken to replicate the retinal scans. Using the imaged micrometer target, the scan dimensions were determined and used to optimize the software model of the OCT scanner. This calibration was performed once to represent the base state of the OCT system.

Regarding the patient eye, a schematic model eye was used as a basis,[30] and for each subject, the model eye was customized by incorporating the subject's corneal curvature, anterior chamber depth (ACD), and axial length (AL) as measured in the SEED study (Zeiss IOLMaster). The model OCT scanner and eye were then combined, and both were optimized together to minimize the spot size across the retina. From this model, the modeled scan beam positions were used to distortion correct the OCT scan. For optical path length to physical distance conversions in the posterior eye OCT image, a presumed uniform refractive index of 1.34 was used.[31] The distortion-corrected right eye RPE segmentation volumes were the final form used for shape analysis.

Shape Analysis

Two forms of shape analysis were performed on the eye images: spherical and aspherical. For spherical analysis, we fit the eye segmentations—both MRI and OCT—to the algebraic equation for a sphere using the least squares method.[32] The specific form was the spherical form of the general quadric surface equation: $A(x^2 + y^2 + z^2) + 2Gx + 2Hx + 2Iz = 1$. The radius of curvature of the fitted sphere (R_c) was used as the spherical shape descriptor.

For aspherical analysis, we fit the eye segmentations to the algebraic equation for an ellipsoid constrained to have its axes aligned to the Cartesian axes using the least squares method.[32] The specific form was $Ax^2 + By^2 + Cz^2 + 2Gx + 2Hx + 2Iz = 1$. However, for the OCT segmentations, there was insufficient information in just the limited, approximately 6- × 6-mm scanned surface to successfully fit an ellipsoid with this equation; instead, the fitting resulted in hyperboloids. To fit to an ellipsoid, additional information was added to further constrain the fitting. Specifically, biometry data available from the distortion correction step was used to create a pilot estimate of the axial radius of curvature: $R_{xz,pilot} = (AL - ACD)/2$. The OCT surface was then reflected across the xy plane. This resulted in a mirrored copy of the OCT surface whose center was 2 * $R_{xz,pilot}$ away from the center of the original OCT surface. This mirroring was done only to enable ellipsoid fitting, which has mirrored symmetry, and was not meant to reflect mirrored biological morphology. With these pilot estimates and constraints, the OCT segmentations could then be fit to an ellipsoid (Fig. 2). For both imaging modalities, the axial asphericity Q_{xz} was defined as $R_x^2/R_z^2 - 1$ where R_x and R_z were the radii in the designated axes for the fitted ellipsoid. Categorical descriptors were assigned using $Q_{xz} > 0$ as oblate and $Q_{xz} < 0$ as prolate. Aspheric descriptors were limited to the xz plane because the segmentations for both OCT and MRI were performed in that plane. While OCT B-scans in the fast axis (xz in this case) are relatively motionless, the orthogonal slow scan axis (yz in this case) would be subject to significant motion artifacts, which could affect shape measurements; OCT scans taken with the fast axis in the yz direction were not available in this dataset.

Statistical Analysis

All statistical analyses were performed in JMP Pro 12.0.1 (SAS Institute, Cary, NC, USA). For numerical comparisons, paired t-tests were performed to compare MRI and OCT measurements of R_c and Q_{xz}. Paired differences between MRI and OCT measurements for the study population were considered statistically significantly different for $P \leq 0.05$. To have 80% power to detect a difference of at least 500 μm between MRI and OCT measures of R_c with $\alpha = 0.05$, a minimum of 48 eyes needed to be analyzed. This difference was appropriate given that the pixel spacing in the MRI images was 1 mm. Additionally, Bland-Altman plots were generated to provide a visual representation of the distribution and the limits of agreement (±1.96 * standard deviation of paired differences).[33]

For categorical comparisons of asphericity (prolate and oblate), overall agreement was calculated as number of matching comparisons divided by the total subjects. Additionally, McNemar's test was performed, and kappa (κ) was used to estimate agreement between MRI and OCT categorical designations of asphericity. Sensitivity and specificity were also calculated for the prolate state using MRI as the gold standard.

Results

The final population consisted of 52 right eyes of 52 subjects (mean ± SD age: 67.8 ± 5.6 years; 16 males, 36 females). The spherical equivalent refraction ranged from +0.50 to −5.38 diopters (D) (mean −0.81 D).

Spherical Shape Analysis

The mean paired difference between MRI and original, non–distortion-corrected OCT measures of R_c was 24.03 ± 46.49 mm ($P = 0.0005$) with limits of agreement of −67.08 and 115.15 mm. After distortion correction of OCT images, the mean paired difference between MRI and OCT measures of R_c was −0.23 ± 2.47 mm ($P = 0.51$) with limits of agreement of −5.06 and 4.61 mm. The distribution of differences in Bland-Altman form is shown in Figure 3, left and center.

Aspherical Shape Analysis

For aspherical analysis, only distortion-corrected OCT images were used because the lower-order spherical fitting (R_c) already showed a substantial difference compared to MRI. The mean paired difference between MRI and distortion-corrected OCT measures of Q_{xz} was −0.052 ± 0.343 ($P = 0.28$) with limits of agreement of −0.7234 and 0.6204. The distribution of differences in Bland-Altman form is shown in Figure 3, right.

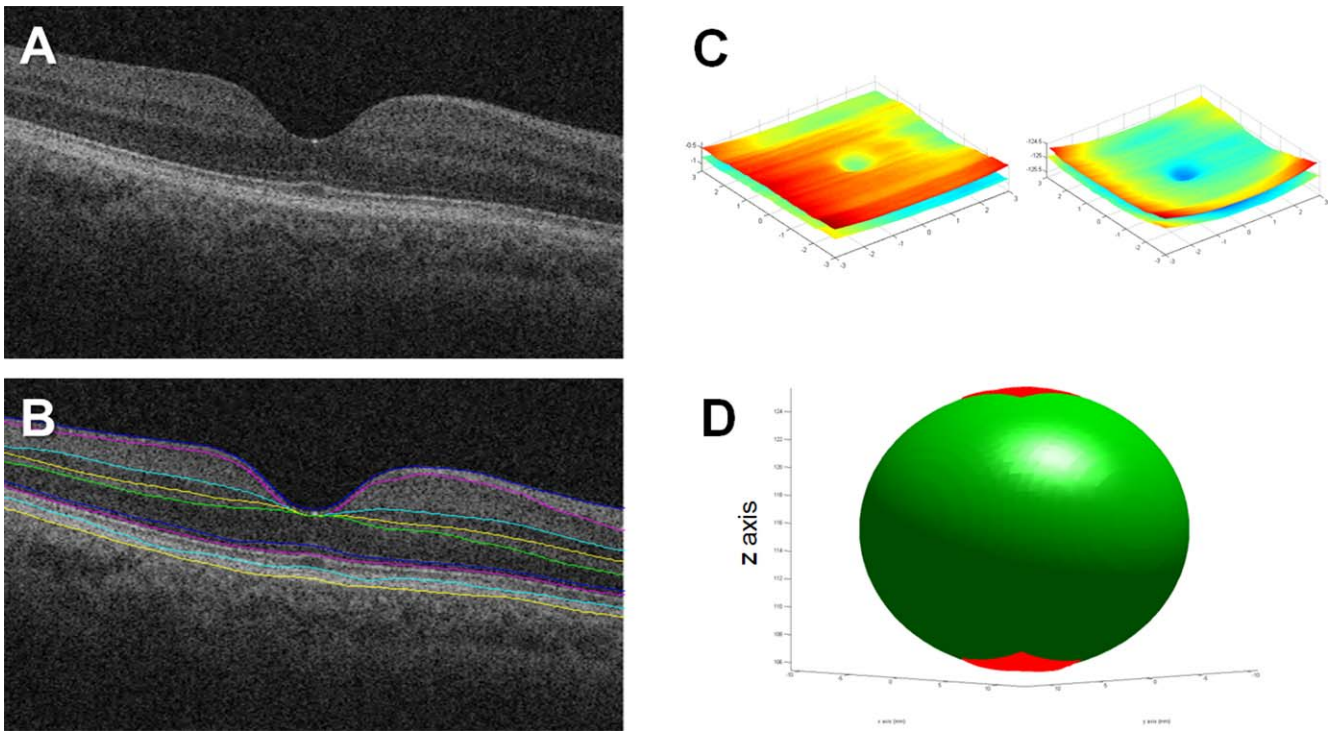

FIGURE 2. Overview of analysis of OCT images. (**A**) Standard view of one representative B-scan from OCT volume of a right eye with the axial dimension stretched per convention. (**B**) Retinal layers were automatically segmented. Only the retinal pigment epithelial layer (*bottom yellow layer*) was used for shape analysis. (**C**) Original (*left*) and distortion-corrected (*right*) retinal surfaces from the volume displayed using isotropic axes. Note the relative flatness of the retina in the original data and the restoration of ocular curvature in the distortion-corrected data. For spherical fitting, these surface data were all that was required. (**D**) Given the limited area covered by the OCT scan, additional pilot estimates were required for successful ellipsoid fitting. Briefly, the corrected retinal surface from (**C**), represented as the *bottom red surface* in (**D**), was mirrored across the *xy* plane and placed [axial length minus anterior chamber depth] away from the original surface. The mirrored surface (represented as the *top red surface* in [**D**]) and the estimate of the *z* radius (represented by half the distance between the two surfaces) allowed for ellipsoid fitting of the OCT data.

Categorically, OCT agreed with MRI classification of oblateness ($Q_{xz} > 1$) and prolateness ($Q_{xz} < 1$) in 47 of 52 eyes for an overall agreement of 90.4%. Within the 49 eyes classified as oblate by MRI, OCT also categorized 44 of those eyes as oblate and misclassified 5 eyes as prolate. Out of 3 eyes that MRI categorized as prolate, OCT also categorized all 3 of those eyes as prolate. Assuming MRI to be the gold standard and "prolate" to be the nonnormal state, the

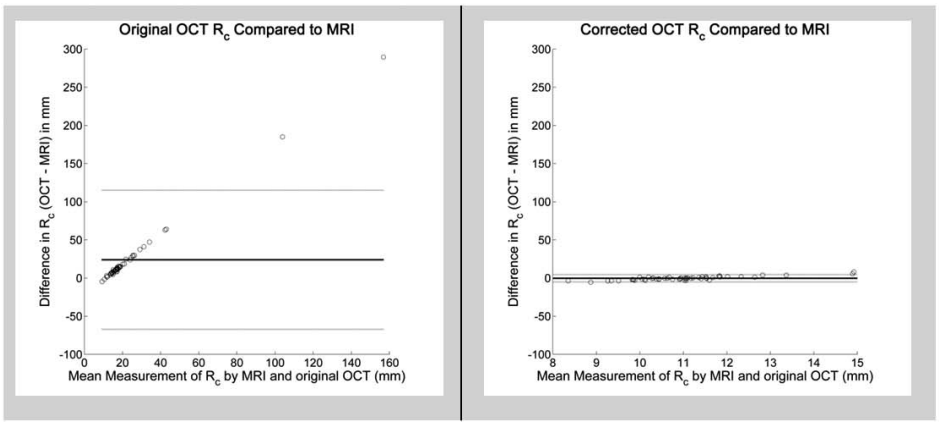

FIGURE 3. Bland-Altman comparison of spherical radius of curvature (R_c) measured by MRI and original uncorrected OCT (*left*) and corrected OCT (*middle*) as well as comparison of asphericity (Q_{xz}) measured by MRI and corrected OCT (*right*). The differences in R_c in mm (*y*-axis) for the *left* and *middle plots* are set to the same scale to facilitate comparison between original and corrected OCT. *Left*: R_c for original OCT versus MRI: The mean difference was 24.03 mm. The Bland-Altman limits of agreement (±1.96× standard deviation of differences, *gray lines*) were –67.08 and 115.15 mm. *Middle*: R_c for corrected OCT versus MRI: The mean difference was –0.22 mm. The limits of agreement were –5.06 and 4.61 mm. Compared to the uncorrected OCT in the *left plot*, the difference and distribution are substantially smaller. *Right*: Q_{xz} for corrected OCT versus MRI: The mean difference was –0.0515. The limits of agreement were –0.7234 and 0.6204.

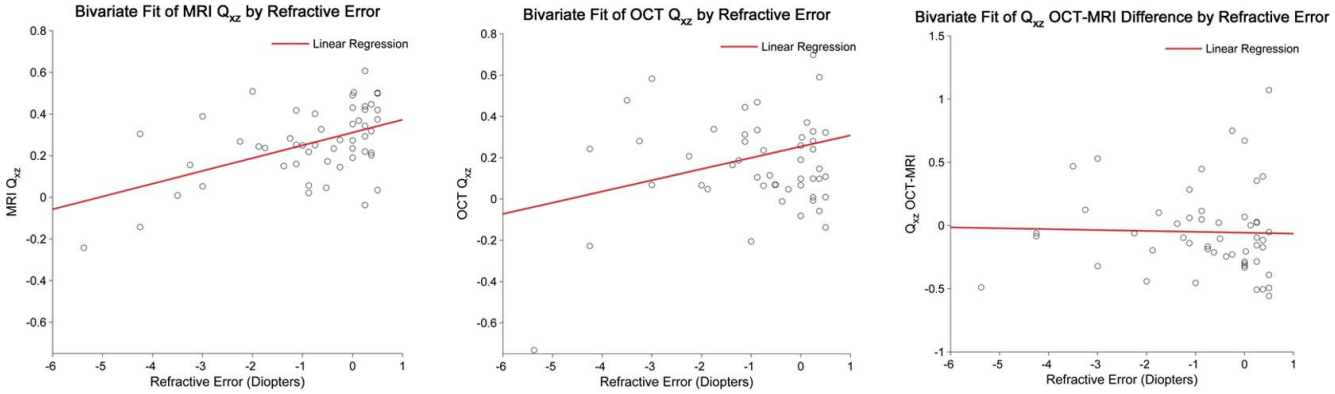

FIGURE 4. Relationship between asphericity (Q_{xz}) and spherical equivalent refractive error as measured by MRI (*left*) and OCT (*center*). The *red lines* are linear regressions with R^2 of 0.25, 0.07, and 0.0009 from *left to right*. Rather than an exact fitting of the data, the linear regressions show the general trend of less oblateness as myopia increases in both MRI and OCT measures of Q_{xz}. The right figure shows the paired differences between OCT measures of Q_{xz} by MRI and OCT as a function of refractive error. Refractive error did not appear to affect the differences between MRI and OCT (slope = –0.06).

resultant sensitivity of OCT for prolateness is 100%, and the specificity of OCT for prolateness is 89.8%. Overall, $\kappa = 0.50$ with 95% bounds of 0.14 to 0.86.

The distributions of $Q_{xz,MRI}$, $Q_{xz,OCT}$, and their paired difference, $\Delta(Q_{xz,OCT} - Q_{xz,MRI})$, as a function of the spherical equivalent refractive error are shown in Figure 4. For MRI, Q_{xz} showed a trend of becoming more prolate as myopia increased. There was a similar trend for OCT. There was no apparent relationship between $\Delta(Q_{xz,OCT} - Q_{xz,MRI})$ and refractive error.

DISCUSSION

Posterior eye shape assessment has been used in the study of myopic refractive error and has been associated with pathologic forms of myopia. The predominant imaging modality used to measure posterior eye shape has been MRI. In contrast to MRI, OCT is far more accessible in eye care settings worldwide, is less invasive, and is less costly than MRI. With correction of optical and display distortions inherent to OCT, we showed that there was no statistically significant difference between MRI- and OCT-measured posterior eye shape as described by spherical radius of curvature. When using higher-order descriptors of posterior eye shape (asphericity, Q), there was similarly no statistically significant difference between the MRI and OCT measures for this population. In prior work,[28] Q_{xz} values by MRI in an emmetropic and myopic population ranged from –0.06 to 0.55, which is consistent with the MRI Q_{xz} values measured in this study. In that same work and others,[8] a trend of decreasing oblateness with increasing myopic refractive error was shown, which was also seen in this study for both MRI and OCT measures of Q_{xz}.

Although there was no statistically significant difference between MRI and OCT measures of asphericity for this population, closer examination of the data revealed important differences if viewed at the individual rather than population level. Even with OCT distortion correction and considering the expected range of Q_{xz} values reported by others, the scale of the standard deviation of the paired differences between MRI and OCT for Q_{xz} is half that range. For eyes classified as oblate by MRI, OCT misclassified 10% of those as prolate. Overall, the classification agreement between MRI and OCT was also merely moderate. Given that there were only three prolate eyes (by MRI) in this study population, OCT performance could potentially differ, be better or worse, with more prolate eyes. The number of prolate eyes seen in this study is consistent with that of prior work, however.[8,28]

There are important limitations to the use of OCT for measuring posterior eye shape. First, these OCT scans were acquired using standard commercial systems and protocols. Were a different OCT system used, potentially even of the same type, specific calibration measurements and models of the system would likely need to be created on a per system basis. There are also useful parameters that cannot currently be obtained from the commercial system. Altering the distance between the eye and OCT system can affect the OCT displayed eye curvature. Ophthalmic photographers often use this knowledge to flatten the retinal OCT image. Knowing the OCT system to eye distance would remove this source of error in the distortion correction algorithms. Also, OCT scans are sequential in time, and patient motion in the scan introduces higher-frequency artifacts into the scans. Spherical and aspherical fittings serve effectively as low-pass filters to mitigate some of the motion artifacts for our analyses; faster OCT image acquisition rates or a dedicated motion correction solution at the time of capture would minimize captured motion artifacts in the actual imaged surface.[34] However, our current use of these global, lower-order shape descriptors (sphere, ellipsoid) does not describe localized deformations. Currently available descriptive classification systems for localized deformations[9] still play a valuable role until numeric methods for identifying localized deformations are developed. Finally, the OCT scans used in this population covered only a 6- × 6-mm area of the back of the eye. This is a small percentage of the surface area of the posterior eye (only 4.3% of the approximately 831 mm^2 for the posterior half of a sphere with radius 11.5 mm). Generating Q_{xz} for OCT in this study required additional biometric data from non-OCT devices and pilot constraints to ensure an ellipsoid fitting; these constraints likely affected the numeric accuracy of the Q_{xz} measurement because of the constraint this imposes on R_{xz}. Direct surface comparison was also not possible as unique registration points were not shared between MRI and OCT (foveal pit present in OCT but not seen in MRI; optic nerve present in MRI but not seen in these macular OCT volumes). Future advances in OCT systems with longer and wider scan ranges such as full eye biometers and wide-field systems will help overcome these current limitations in scan range.[35–40] Minor adjustments would need to be considered in wide-field OCT scans for features such as optic nerve head. Automated methods[41,42] can be used to detect and exclude this known, localized

deformation prior to global shape fitting of the posterior eye. Overall, though, because the algorithms and analyses used in this study should be conceptually generalizable to any OCT system, they can be adapted to take advantage of future improvements in OCT hardware.

It is important to note that although MRI has been used in multiple studies as the standard for measuring eye shape,[6–8,12,13,26,28] MRI can itself be subject to inaccuracies besides uncertainties from resolution limits. Geometric distortions in MRI images result from magnetic gradient field nonlinearities and magnetic field inhomogeneities.[43,44] Gradient field nonlinearities create increasing distortions away from the gradient isocenter of the MRI coils; the effect on the image is akin to radial distortions (e.g. pincushion) encountered in optical imaging. Simultaneous excitation of the whole field of view using 3D MRI reduces the presence of some types of nonlinear gradient aberrations that are secondary to 2D slice-based imaging. To compensate for the continued presence of barrel aberration in 3D MRI, calibration and mathematical/software techniques are used in the acquisition process. Effects of gradient nonlinearity can also be reduced by placing the region of interest close to the 3D isocenter of the gradient coils. In regard to magnetic field inhomogeneities, inhomogeneities create geometric distortions as well as artifactual intensity variations in the image. Inhomogeneities originate from the scanner and interactions of the magnetic field with the imaged object. Inhomogeneities are particularly prominent at interfaces with large differences in magnetic susceptibility like air to tissue or paramagnetic substances such as iron in tissue. General scanner inhomogeneities are addressed using shimming, resistive coils that generate compensatory fields to counter magnetic field inhomogeneities that are automatically performed in modern scanners. While there are additional advanced techniques to address magnetic field inhomogeneities outside the scope of this current work, the general idea is that areas with large differences in magnetic susceptibility, such as the anterior eye, are prone to inaccuracies. With respect to the current work, the location of the eye near the *z*-axis center of the 3D MRI volume and analysis of only the posterior eye surrounded by tissue are advantageous. In the *xz* plane, the posterior eye is peripheral to the center of the slice, and uncompensated gradient nonlinearities could affect the accuracy of the spatial measurements of our standard. In the stereotactic surgery community, computed tomography (CT) is generally regarded as the more spatially accurate modality.[45] Studies comparing eye shape with MRI and CT remain to be done.

Other methods besides MRI and OCT to measure posterior eye shape have been described. These include ultrasound, peripheral refraction, and partial coherence interferometry (PCI).[26,46–49] Despite its long history in eye care, there are few studies using ultrasound for measuring posterior eye shape (excepting 1-dimensional length measurements) and no comparisons of this type of measurement to other imaging modalities like MRI. The peripheral refraction method and PCI require dedicated hardware customizations; they also have limited sampling as measurements have to be specifically made at defined points to recreate the posterior eye surface. Aside from those caveats, those methods are acceptable ways to determine posterior eye shape. Comparatively, the OCT data used in this study were from an unmodified commercial system, and the data representing the surface were acquired in a single, seconds-long scan. Further, in addition to prospective acquisitions, OCT datasets acquired in the past under standard clinical conditions, as used in this study, can be analyzed to recover shape measures with the earlier considerations.

In conclusion, we have demonstrated that with careful calibration of the OCT scanner enabling correction of optical and display artifacts, OCT measures of posterior eye shape by spherical and aspherical descriptors are fairly accurate when compared with MRI measures of the same eyes across a population. On an individual level, however, there is not perfect agreement between these modalities for aspherical classification. This is one of the first comparisons of OCT to other medical imaging modalities and may allow posterior eye shape determinations to be more readily available for both researchers and clinicians. This use of OCT imaging to study posterior eye shape can potentially lead to better assessment and understanding of myopia.

Acknowledgments

The authors thank Stephanie J. Chiu, PhD (Duke Reading Center), for her assistance with the automatic retinal segmentation software; Jason Chia (Singapore Eye Research Institute) for his assistance in organizing the OCT and biometry data; Sandra S. Stinnett (Duke University) for her assistance with statistical analysis; and Yueh Z. Lee (University of North Carolina-Chapel Hill), G. Allan Johnson (Duke University), and Kevin Chan (University of Pittsburgh) for their helpful discussions on MRI physics.

Presented in part at the Asia-ARVO meeting, Yokohama, Japan, February 16–19, 2015.

Supported in part by Grants R01-EY024312 (ANK) and R01-EY014685 (TLY) from the National Institutes of Health (Bethesda, MD, USA) and Research to Prevent Blindness, Inc. (New York, NY, USA). The authors alone are responsible for the content and writing of the paper.

Disclosure: **A.N. Kuo**, None; **P.K. Verkicharla**, None; **R.P. McNabb**, None; **C.Y. Cheung**, None; **S. Hilal**, None; **S. Farsiu**, P; **C. Chen**, None; **T.Y. Wong**, None; **M.K. Ikram**, None; **C.Y. Cheng**, None; **T.L. Young**, None; **S.M. Saw**, None; **J.A. Izatt**, Zeiss (R), Leica (R), P

References

1. Vitale S, Ellwein L, Cotch MF, Ferris FL III, Sperduto R. Prevalence of refractive error in the United States, 1999-2004. *Arch Ophthalmol*. 2008;126:1111–1119.
2. Jung SK, Lee JH, Kakizaki H, Jee D. Prevalence of myopia and its association with body stature and educational level in 19-year-old male conscripts in Seoul, South Korea. *Invest Ophthalmol Vis Sci*. 2012;53:5579–5583.
3. Pan CW, Zheng YF, Anuar AR, et al. Prevalence of refractive errors in a multiethnic Asian population: the Singapore epidemiology of eye disease study. *Invest Ophthalmol Vis Sci*. 2013;54:2590–2598.
4. Pan CW, Klein BE, Cotch MF, et al. Racial variations in the prevalence of refractive errors in the United States: the multi-ethnic study of atherosclerosis. *Am J Ophthalmol*. 2013;155:1129–1138.
5. Pan CW, Dirani M, Cheng CY, Wong TY, Saw SM. The age-specific prevalence of myopia in Asia: a meta-analysis. *Optom Vis Sci*. 2015;92:258–266.
6. Atchison DA, Jones CE, Schmid KL, et al. Eye shape in emmetropia and myopia. *Invest Ophthalmol Vis Sci*. 2004;45:3380–3386.
7. Beenakker JW, Shamonin DP, Webb AG, Luyten GP, Stoel BC. Automated retinal topographic maps measured with magnetic resonance imaging. *Invest Ophthalmol Vis Sci*. 2015;56:1033–1039.
8. Gilmartin B, Nagra M, Logan NS. Shape of the posterior vitreous chamber in human emmetropia and myopia. *Invest Ophthalmol Vis Sci*. 2013;54:7240–7251.

9. Moriyama M, Ohno-Matsui K, Hayashi K, et al. Topographic analyses of shape of eyes with pathologic myopia by high-resolution three-dimensional magnetic resonance imaging. *Ophthalmology*. 2011;118:1626–1637.
10. Wong TY, Ferreira A, Hughes R, Carter G, Mitchell P. Epidemiology and disease burden of pathologic myopia and myopic choroidal neovascularization: an evidence-based systematic review. *Am J Ophthalmol*. 2014;157:9–25.
11. Ohno-Matsui K, Kawasaki R, Jonas JB, et al. International photographic classification and grading system for myopic maculopathy. *Am J Ophthalmol*. 2015;159:877–883.
12. Cheng HM, Singh OS, Kwong KK, Xiong J, Woods BT, Brady TJ. Shape of the myopic eye as seen with high-resolution magnetic resonance imaging. *Optom Vis Sci*. 1992;69:698–701.
13. Lim LS, Chua S, Tan PT, et al. Eye size and shape in newborn children and their relation to axial length and refraction at 3 years. *Ophthalmic Physiol Opt*. 2015;35:414–423.
14. Huang D, Swanson EA, Lin CP, et al. Optical coherence tomography. *Science*. 1991;254:1178–1181.
15. Swanson EA. OCT technology transfer and the OCT market. In: Drexler W, Fujimoto JG, eds. *Optical Coherence Tomography*. New York: Springer; 2015:2529–2571.
16. Westphal V, Rollins A, Radhakrishnan S, Izatt J. Correction of geometric and refractive image distortions in optical coherence tomography applying Fermat's principle. *Opt Express*. 2002;10:397–404.
17. Zawadzki RJ, Fuller AR, Choi SS, Wiley DF, Hamann B, Werner JS. Correction of motion artifacts and scanning beam distortions in 3D ophthalmic optical coherence tomography imaging. *Proc SPIE* 6426, Ophthalmic Technologies XVII, 642607. 2007. doi:10.1117/12.701524
18. Podoleanu A, Charalambous I, Plesea L, Dogariu A, Rosen R. Correction of distortions in optical coherence tomography imaging of the eye. *Phys Med Biol*. 2004;49:1277–1294.
19. Ortiz S, Siedlecki D, Grulkowski I, et al. Optical distortion correction in optical coherence tomography for quantitative ocular anterior segment by three-dimensional imaging. *Opt Express*. 2010;18:2782–2796.
20. Kuo AN, McNabb RP, Chiu SJ, et al. Correction of ocular shape in retinal optical coherence tomography and effect on current clinical measures. *Am J Ophthalmol*. 2013;156:304–311.
21. Chua J, Koh JY, Tan AG, et al. Ancestry, socioeconomic status, and age-related cataract in Asians: the Singapore Epidemiology of Eye Diseases Study. *Ophthalmology*. 2015;122:2169–2178.
22. Hilal S, Ikram MK, Saini M, et al. Prevalence of cognitive impairment in Chinese: epidemiology of dementia in Singapore study. *J Neurol Neurosurg Psychiatry*. 2013;84:686–692.
23. Ong YT, Hilal S, Cheung CY, et al. Retinal neurodegeneration on optical coherence tomography and cerebral atrophy. *Neurosci Lett*. 2015;584:12–16.
24. Hilal S, Tan CS, Xin S, et al. Prevalence of cognitive impairment and dementia in Malays - Epidemiology of Dementia in Singapore Study [published online ahead of print October 2, 2015]. *Curr Alzheimer Res*. doi:10.2174/1567205012666151002123813.
25. Wang L, He L, Mishra A, Li C. Active contours driven by local Gaussian distribution fitting energy. *Signal Processing*. 2009;89:2435–2447.
26. Verkicharla PK, Suheimat M, Pope JM, et al. Validation of a partial coherence interferometry method for estimating retinal shape. *Biomed Opt Express*. 2015;6:3235–3247.
27. Berrio E, Tabernero J, Artal P. Optical aberrations and alignment of the eye with age. *J Vis*. 2010;10(14):34. doi:10.1167/10.14.34.
28. Atchison DA, Pritchard N, Schmid KL, Scott DH, Jones CE, Pope JM. Shape of the retinal surface in emmetropia and myopia. *Invest Ophthalmol Vis Sci*. 2005;46:2698–2707.
29. Chiu SJ, Li XT, Nicholas P, Toth CA, Izatt JA, Farsiu S. Automatic segmentation of seven retinal layers in SDOCT images congruent with expert manual segmentation. *Opt Express*. 2010;18:19413–19428.
30. Goncharov AV, Dainty C. Wide-field schematic eye models with gradient-index lens. *J Opt Soc Am A Opt Image Sci Vis*. 2007;24:2157–2174.
31. Drexler W, Hitzenberger CK, Baumgartner A, Findl O, Sattmann H, Fercher AF. Investigation of dispersion effects in ocular media by multiple wavelength partial coherence interferometry. *Exp Eye Res*. 1998;66:25–33.
32. Petrov Y. Ellipsoid fit. MATLAB Central. Available at: http://www.mathworks.com/matlabcentral/fileexchange/24693-ellipsoid-fit. Accessed November 8, 2015.
33. Bland JM, Altman DG. Statistical methods for assessing agreement between two methods of clinical measurement. *Lancet*. 1986;1:307–310.
34. Kraus MF, Potsaid B, Mayer MA, et al. Motion correction in optical coherence tomography volumes on a per A-scan basis using orthogonal scan patterns. *Biomed Opt Express*. 2012;3:1182–1199.
35. Dhalla AH, Nankivil D, Bustamante T, Kuo A, Izatt JA. Simultaneous swept source optical coherence tomography of the anterior segment and retina using coherence revival. *Opt Lett*. 2012;37:1883–1885.
36. Ruggeri M, Uhlhorn SR, De Freitas C, Ho A, Manns F, Parel JM. Imaging and full-length biometry of the eye during accommodation using spectral domain OCT with an optical switch. *Biomed Opt Express*. 2012;3:1506–1520.
37. Grulkowski I, Liu JJ, Potsaid B, et al. Retinal, anterior segment and full eye imaging using ultrahigh speed swept source OCT with vertical-cavity surface emitting lasers. *Biomed Opt Express*. 2012;3:2733–2751.
38. Zhong J, Tao A, Xu Z, et al. Whole eye axial biometry during accommodation using ultra-long scan depth optical coherence tomography. *Am J Ophthalmol*. 2014;157:1064–1069.
39. Kolb JP, Klein T, Kufner CL, Wieser W, Neubauer AS, Huber R. Ultra-widefield retinal MHz-OCT imaging with up to 100 degrees viewing angle. *Biomed Opt Express*. 2015;6:1534–1552.
40. McNabb RP, Grewal DS, Mehta R, et al. Wide field of view swept-source optical coherence tomography for peripheral retinal disease [published online ahead of print January 11, 2016]. *Br J Ophthalmol*. doi:10.1136/bjophthalmol-2015-307480.
41. Srinivasan PP, Heflin SJ, Izatt JA, Arshavsky VY, Farsiu S. Automatic segmentation of up to ten layer boundaries in SD-OCT images of the mouse retina with and without missing layers due to pathology. *Biomed Opt Express*. 2014;5:348–365.
42. Almobarak FA, O'Leary N, Reis AS, et al. Automated segmentation of optic nerve head structures with optical coherence tomography. *Invest Ophthalmol Vis Sci*. 2014;55:1161–1168.
43. Sumanaweera TS, Adler JR Jr, Napel S, Glover GH. Characterization of spatial distortion in magnetic resonance imaging and its implications for stereotactic surgery. *Neurosurgery*. 1994;35:696–703, discussion 703–704.
44. Wang D, Strugnell W, Cowin G, Doddrell DM, Slaughter R. Geometric distortion in clinical MRI systems Part I: evaluation using a 3D phantom. *Magn Reson Imaging*. 2004;22:1211–1221.

Investigative Ophthalmology & Visual Science

45. Yu C, Apuzzo ML, Zee CS, Petrovich Z. A phantom study of the geometric accuracy of computed tomographic and magnetic resonance imaging stereotactic localization with the Leksell stereotactic system. *Neurosurgery*. 2001;48:1092–1098, discussion 1098–1099.
46. Fledelius HC, Goldschmidt E. Eye shape and peripheral visual field recording in high myopia at approximately 54 years of age, as based on ultrasonography and Goldmann kinetic perimetry. *Acta Ophthalmol*. 2010;88:521–526.
47. Dunne MC. A computing scheme for determination of retinal contour from peripheral refraction, keratometry and A-scan ultrasonography. *Ophthalmic Physiol Opt*. 1995;15:133–143.
48. Verkicharla PK, Mathur A, Mallen EA, Pope JM, Atchison DA. Eye shape and retinal shape, and their relation to peripheral refraction. *Ophthalmic Physiol Opt*. 2012;32:184–199.
49. Schmid GF. Axial and peripheral eye length measured with optical low coherence reflectometry. *J Biomed Opt*. 2003;8:655–662.

Investigative Ophthalmology & Visual Science